entropy

MDPI

Article

Microstructures of $Al_{7.5}Cr_{22.5}Fe_{35}Mn_{20}Ni_{15}$ High-Entropy Alloy and Its Polarization Behaviors in Sulfuric Acid, Nitric Acid and Hydrochloric Acid Solutions

Chun-Huei Tsau * and Po-Yen Lee

Institute of Nanomaterials, Chinese Culture University, Taipei 11114, Taiwan; Smile_DinDin@hotmail.com
* Correspondence: chtsau@staff.pccu.edu.tw; Tel.: +886-2-2861-0511 (ext. 33621); Fax: +886-2-2861-8287

Academic Editor: An-Chou Yeh
Received: 15 June 2016; Accepted: 1 August 2016; Published: 8 August 2016

Abstract: This paper investigates the microstructures and the polarization behaviors of $Al_{7.5}Cr_{22.5}Fe_{35}Mn_{20}Ni_{15}$ high-entropy alloy in 1M (1 mol/L) deaerated sulfuric acid (H_2SO_4), nitric acid (HNO_3), and hydrochloric acid (HCl) solutions at temperatures of 30–60 °C. The three phases of the $Al_{7.5}Cr_{22.5}Fe_{35}Mn_{20}Ni_{15}$ high-entropy alloy are body-centered cubic (BCC) dendrites, face-centered cubic (FCC) interdendrites, and ordered BCC precipitates uniformly dispersed in the BCC dendrites. The different phases were corroded in different acidic solutions. The passivation regions of the $Al_{7.5}Cr_{22.5}Fe_{35}Mn_{20}Ni_{15}$ alloy are divided into three and two sub-regions in the solutions of H_2SO_4 and HNO_3 at 30–60 °C, respectively. The passivation region of the $Al_{7.5}Cr_{22.5}Fe_{35}Mn_{20}Ni_{15}$ alloy is also divided into two sub-domains in 1M deaerated HCl solution at 30 °C. The $Al_{7.5}Cr_{22.5}Fe_{35}Mn_{20}Ni_{15}$ alloy has almost equal corrosion resistance in comparison with 304 stainless steel (304SS) in both the 1M H_2SO_4 and 1M HCl solutions. The polarization behaviors indicated that the $Al_{7.5}Cr_{22.5}Fe_{35}Mn_{20}Ni_{15}$ alloy possessed much better corrosion resistance than 304SS in 1M HNO_3 solution. However, in 1M NaCl solution, the corrosion resistance of the $Al_{7.5}Cr_{22.5}Fe_{35}Mn_{20}Ni_{15}$ alloy was less than 304SS.

Keywords: $Al_{7.5}Cr_{22.5}Fe_{35}Mn_{20}Ni_{15}$ alloy; high-entropy alloy; microstructure polarization curve; sulfuric acid; nitric acid; hydrochloric acid

1. Introduction

High-entropy alloys are alloys that have more than four elements, and the content of each element is in the range of 5–35 atomic percent. Because high-entropy alloys contain many major elements, their properties are thus not dominated by any one element. This concept was first proposed by Yeh et al. [1–3]. Yeh has independently explored this concept since 1995, with the first paper being published in 2004 [1]. The concept of high-entropy alloys is now widely known. Zhang et al. also investigated how to predict high-entropy phase formation and how to design alloys, and proposed some guidelines for the prediction of phase formation [4]. The high-entropy alloy concept is not only used in typical alloy systems, but also extends to thin film procedures [5,6], refectory materials [7,8], and is also used to develop bulk metallic glasses [9]. Aside from the mechanical properties of high-entropy alloys that are investigated, their corrosion behaviors are also studied [10–12].

The Al-Cr-Fe-Mn-Ni alloy system is one of the high-entropy alloy systems developed by the Yeh group. For example, $Al_xCrFe_{1.5}MnNi_{0.5}$ alloys [13] possess good workability, precipitation hardening, and high-temperature oxidation resistance. The hardness of both $Al_{0.3}CrFe_{1.5}MnNi_{0.5}$ and $Al_{0.5}CrFe_{1.5}MnNi_{0.5}$ alloys is higher than HV950 after aging treatment. The workability of $Al_5Cr_{12}Fe_{35}Mn_{28}Ni_{20}$ alloy [3] is also very good in both the as-cast and as-homogenized states;

this alloy can be cold rolled to an extension of 4257% without any edge cracking. Moreover, the enhanced pitting corrosion resistance of anodic treated $Al_xCrFe_{1.5}MnNi_{0.5}$ (x = 0, 0.3, 0.5) alloys in H_2SO_4 solution has been investigated [14]. The results reveal that the surface of the anodic treated $Al_{0.3}CrFe_{1.5}MnNi_{0.5}$ alloy has a stable passive oxide film, which effectively protects against pitting corrosion in 15% sulfuric acid solution. In this study, the experimental alloy, $Al_{7.5}Cr_{22.5}Fe_{35}Mn_{20}Ni_{15}$, is modified from the $Al_xCrFe_{1.5}MnNi_{0.5}$ alloy to change the ratio of body-centered cubic (BCC) dendrites and face-centered cubic (FCC) interdendrites. This paper studies the microstructures of the $Al_{7.5}Cr_{22.5}Fe_{35}Mn_{20}Ni_{15}$ alloy, and its polarization behaviors in 1M sulfuric acid (H_2SO_4), nitric acid (HNO_3) and hydrochloric acid (HCl) solutions. Also, the results were compared with commercial 304 stainless steel (304SS).

2. Experimental

The $Al_{7.5}Cr_{22.5}Fe_{35}Mn_{20}Ni_{15}$ alloy studied in this paper was received from the Yeh group. The $Al_{7.5}Cr_{22.5}Fe_{35}Mn_{20}Ni_{15}$ alloy were first prepared by arc melting using appropriate amounts of pure elements with purity higher than 99.9%. After that, the alloy was hot forged at 1200 °C and air cooled to room temperature. Then the alloy was warm rolled at 500 °C until the thickness reached 2 mm. Finally, the alloy was annealed at 700 °C for 4 h. The compositions of the $Al_{7.5}Cr_{22.5}Fe_{35}Mn_{20}Ni_{15}$ alloy phases analyzed by Scanning Electron Microscope (SEM, JEOL Ltd., Tokyo, Japan) and Energy Dispersive Spectroscopy (EDS, JEOL Ltd., Tokyo, Japan) are listed in Table 1. The structures were characterized by X-ray diffraction (XRD) using a Rigagu ME510-FM2 (Rigagu Ltd., Tokyo, Japan) with Cu-Kα (λ = 0.1541 nm) radiation operated at 30 kV. The microstructural evolution of the alloy was monitored using a scanning electron microscope (SEM) and a transmission electron microscope (TEM, JEOL Ltd., Tokyo, Japan). SEM observations were made using a JEOL JSM-6335 field emission scanning electron microscope operated at 15 kV. Samples were metallographically prepared and electrochemically etched in 1M H_2SO_4 solution operated at a potential of 2 V. TEM observations were made using a JEOL JEM-3000F high resolution transmission electron microscope operated at 300 kV. The corresponding selected area diffraction patterns (SAD) were calculated from the high resolution lattice image by fast Fourier transforms (FFT) in Gatan digital micrograph software. Thin foil specimens for TEM observation were electrochemically prepared in a digital Fischione twin-jet electropolisher, model 110, in a solution of 10 vol.% perchloric acid and 90 vol.% methanol at a potential of 30 V.

Table 1. Compositions (atomic percent) of the phases in $Al_{7.5}Cr_{22.5}Fe_{35}Mn_{20}Ni_{15}$ high entropy alloy analyzed by SEM/EDS.

Phases	Al	Cr	Fe	Mn	Ni
Overall	8	22	36	18	16
Precipitate	20	8	10	19	43
Interdendrite	6	15	40	23	16
Dendrite	6	28	34	23	8

The polarization curves of the alloys were measured in a Autolab PGSTAT302N potentiostat/galvanostat (Metrohm Autolab B.V., Utrecht, Netherlands) and a three-electrode system at a scanning rate of 1 mV/s. The test temperature range was 30–60 °C in steps of 10 °C. The alloy characteristics were determined, such as corrosion potential (E_{corr}), corrosion current density (i_{corr}), primary passivation potential (E_{pp}, the potential of the first anodic peak), anodic critical current density of the primary anodic peak (i_{pp}), secondary passivation potential (E_{sp}, the potential of the second anodic peak), anodic critical current density of secondary anodic peak (i_{sp}), third passivation potential (E_{tp}, the potential of the third anodic peak), anodic critical current density of the third anodic peak (i_{tp}), passive current density (i_{pass}), and breakdown potential (E_b). The results were also compared with the properties of commercial 304 stainless steel (304SS), which has a composition in weight percent of 71.61% Fe, 18.11% Cr, 8.24% Ni, 1.12% Mn, 0.75% Si, 0.05% Co, 0.02% Mo, 0.05% C, 0.03% P, and 0.02% S.

Specimens for polarization tests were mounted in epoxy resin, and the exposed surface area of the specimens were fixed at 0.1964 cm^2 (0.5 cm in diameter). The reference electrode was a saturated silver chloride electrode (Ag/AgCl), and a smooth Pt sheet was used as the counter electrode. All the values of potential given below are expressed on the saturated silver chloride electrode (SSE), whose reduction potential is 222 mV higher than that on the standard hydrogen electrode (SHE) scale at 25 °C [15,16]. The specimens for measuring the polarization curves were all mechanically wet polished with 1200 SiC grit paper. The test solutions of 1M concentration were prepared from reagent-grade sulfuric acid, nitric acid, hydrochloric acid and sodium chloride, dissolved in distilled water. To eliminate the effect of dissolved oxygen, the solutions were deaerated by bubbling nitrogen gas through the solution prior to and during the polarization experiments.

3. Results and Discussion

The as-cast $Al_{7.5}Cr_{22.5}Fe_{35}Mn_{20}Ni_{15}$ alloy has a dendritic microstructure, but its morphology changes during hot forging, warm rolling, and subsequent annealing. Therefore, some interdendrite fragments are broken and dispersed into the dendrite matrix during deformation. Figure 1 displays the low- and high-magnitude SEM micrographs of the as-received $Al_{7.5}Cr_{22.5}Fe_{35}Mn_{20}Ni_{15}$ alloy. Large amounts of submicron precipitates are present in the dendrite. In addition, a portion of the interdendrite fragments still arranges in lines, and a portion of the interdendrite fragments randomly distributes within the dendrite. Table 1 lists the compositions of the phases in $Al_{7.5}Cr_{22.5}Fe_{35}Mn_{20}Ni_{15}$ alloy; the precipitates are a NiAl-rich phase, the interdendrites are an FeMn-rich phase, and the dendrites are a CrFeMn-rich phase. Figure 2 shows the XRD pattern of the $Al_{7.5}Cr_{22.5}Fe_{35}Mn_{20}Ni_{15}$ alloy, and only two phases are detected. One is a BCC phase with a lattice constant of 0.287 nm; and the other is an FCC phase with a lattice constant of 0.360 nm. Apparently, the BCC phase is the dendrite matrix and the FCC phase is the interdendrite by comparing the intensities of the XRD peaks and the SEM micrograph. This is also later proven by the TEM observation described below.

TEM observation of the $Al_{7.5}Cr_{22.5}Fe_{35}Mn_{20}Ni_{15}$ alloy is shown in Figure 3. Figure 3a is a bright field (BF) image of the dendrite; there are several precipitates dispersed in the dendrite matrix. The matrix evidently shows a cell structure because of recovery during the annealing process after hot working. Moreover, the alloy was annealed at 700 °C for 4 h after hot working; this cell structure indicates that the annealing conditions were not enough for full annealing. Figure 3b is a high-magnitude BF image of a dendrite; the inserts are the corresponding lattice image taken from the [001] direction and the SAD from FFT, which indicates a BCC structure. Figure 3c is a BF image of an interdendrite; the inserts are the corresponding lattice image taken from the [011] direction and the SAD from FFT, which indicates an FCC structure. All of these TEM micrographs were proof of the description above, that dendrites have a BCC structure and that interdendrites have a FCC structure. Figure 3d is a BF image of a precipitate; inserts are the corresponding lattice image taken from the [001] direction and the SAD from FFT, which indicates an ordered BCC structure. Figure 3e is the lattice image taken from the [001] direction of an ordered BCC precipitate, which shows the interface between the precipitate and the dendrite matrix. The upper-left portion is the ordered BCC precipitate, and the lower-right portion is the BCC dendrite. The insert is the corresponding SAD from FFT. The interface shown is almost perfectly coherent.

Figure 4 shows the polarization behaviors of the $Al_{7.5}Cr_{22.5}Fe_{35}Mn_{20}Ni_{15}$ alloy in 1M deaerated H_2SO_4 solution and the SEM micrograph of the alloy after the polarization test. Figure 4a shows the polarization curves of the $Al_{7.5}Cr_{22.5}Fe_{35}Mn_{20}Ni_{15}$ alloy in 1M H_2SO_4 solution at different temperatures. Table 2 presents the data from which the curves are plotted. The E_{corr} of the $Al_{7.5}Cr_{22.5}Fe_{35}Mn_{20}Ni_{15}$ alloy was almost temperature-independent, and stayed at about −0.5 V (SSE) at this temperature range of 30 to 60 °C. However, the i_{corr} increased from 0.13 to 7.28 mA/cm^2 as the temperature increased from 30 to 60 °C, indicating that the reaction was sensitive to temperature. Subsequently, three anodic peaks were observed in each polarization curve; the passivation range for each curve was thus divided into three sub-domains. Abdallah studied the corrosion behavior

of 304SS in 0.5M H_2SO_4 solution, and described that the formation of the three anodic peaks was due to the iron, cobalt, and nickel hydroxide formation that occurred through the dissolution and precipitation mechanism [17]. The first anodic peak of 304SS in 0.5M H_2SO_4 solution was due to the formation of iron hydroxide; the secondary anodic peak was due to the formation of higher oxides of iron and chromium [17,18]; and the third anodic peak was due to the formation of iron, cobalt, and nickel oxyhydroxides [19]. The contents of iron, chromium, and nickel in the $Al_{7.5}Cr_{22.5}Fe_{35}Mn_{20}Ni_{15}$ alloy are more than 74 weight percent, and this study suggests the formation of the three anodic peaks is also due to this similar reason.

The passivation potential and the anodic critical current density for the primary, secondary, and third anodic peaks (i.e., E_{pp}, i_{pp}, E_{sp}, i_{sp}, E_{tp}, and i_{tp}) of the $Al_{7.5}Cr_{22.5}Fe_{35}Mn_{20}Ni_{15}$ alloy are listed in Table 2. The E_{pp} and E_{sp} of the alloy were not sensitive to the temperature, but the E_{tp} increased with increasing temperature. All the anodic critical current densities (i_{pp}, i_{sp}, and i_{tp}) increased significantly with increasing temperature. However, the main passivation region for each polarization curve was located in the region between the secondary and the third anodic peaks, because the extent of passivity of this region was the broadest among these three sub-domains. The E_b of the main passivation regions for all of the polarization curves did not change with temperature and held the same value of 0.98 V (SSE). The passive current density (i_{pass}) of the main passivation regions only slightly increased from 0.03 to 0.09 mA/cm^2 with increasing temperature from 30 to 60 °C.

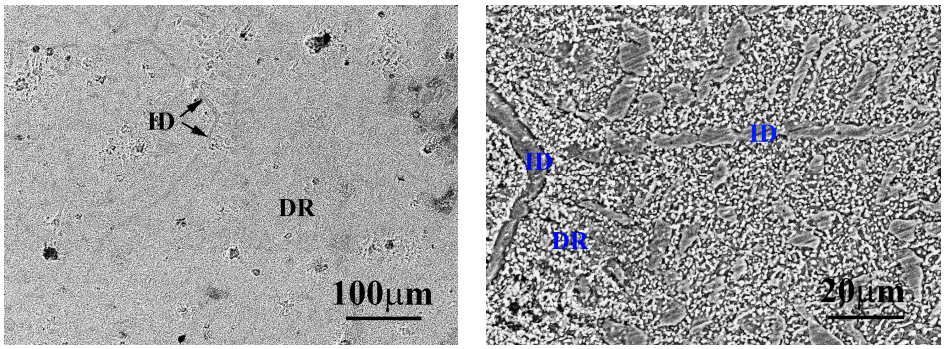

Figure 1. SEM micrographs of the as-received $Al_{7.5}Cr_{22.5}Fe_{35}Mn_{20}Ni_{15}$ alloy at (**a**) low-magnitude, and (**b**) high-magnitude. Marks of DR and ID indicate the dendrite and interdendrite of the alloy, respectively.

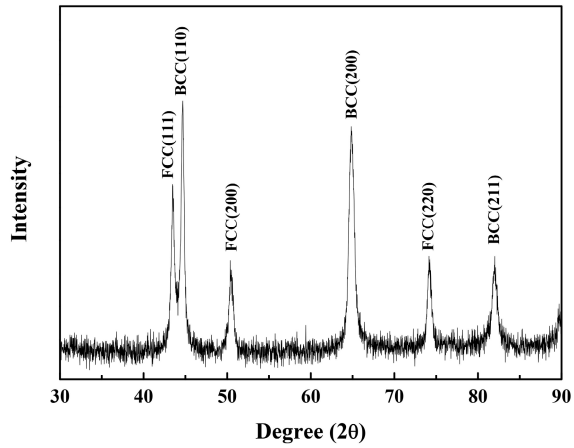

Figure 2. XRD pattern of the $Al_{7.5}Cr_{22.5}Fe_{35}Mn_{20}Ni_{15}$ alloy.

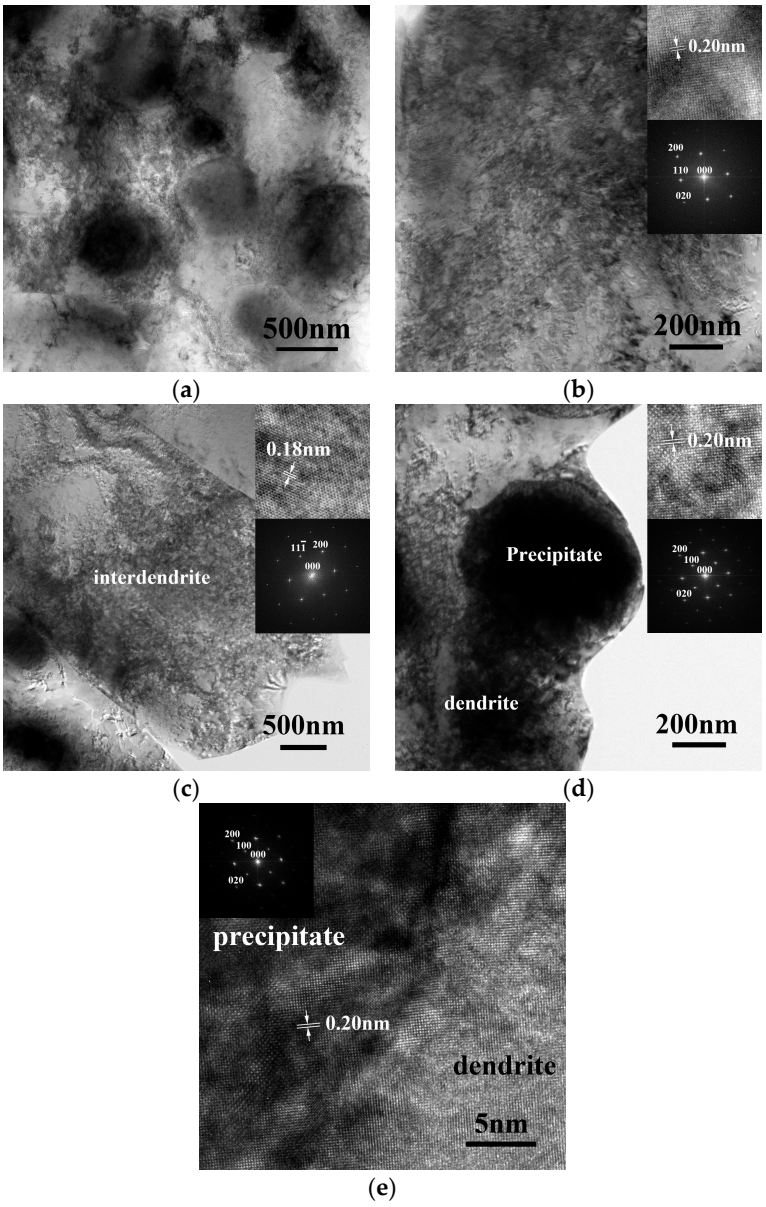

Figure 3. TEM micrographs of the $Al_{7.5}Cr_{22.5}Fe_{35}Mn_{20}Ni_{15}$ alloy: (**a**) a BF image of the dendrite, which shows several precipitates dispersed in the dendrite matrix; (**b**) a BF image of the dendrite, inserts are the corresponding lattice image and SAD taken from the [001] direction; (**c**) a BF image of the interdendrite, inserts are the corresponding lattice image and SAD taken from the [011] direction; (**d**) a BF image of the precipitate, inserts are the corresponding lattice image and SAD taken from the [001] direction; and (**e**) a high resolution lattice image taken from the [001] direction of the interface between the precipitate and dendrite matrix.

Figure 4b compares the polarization curves of the $Al_{7.5}Cr_{22.5}Fe_{35}Mn_{20}Ni_{15}$ alloy and 304SS in 1M H_2SO_4 solution at 30 °C. The E_{corr} for 304SS, −0.32 V (SSE), was higher than that of the $Al_{7.5}Cr_{22.5}Fe_{35}Mn_{20}Ni_{15}$ alloy; and the i_{corr} for 304SS, 0.03 mA/cm^2, was lower than that of the $Al_{7.5}Cr_{22.5}Fe_{35}Mn_{20}Ni_{15}$ alloy. Both the E_{corr} and i_{corr} indicated that the 304SS was nobler than the $Al_{7.5}Cr_{22.5}Fe_{35}Mn_{20}Ni_{15}$ alloy; this is due to the fact that the elements of aluminum and manganese are more active than iron, chromium, and nickel which are the major elements of 304SS. However, the main passivation region of the $Al_{7.5}Cr_{22.5}Fe_{35}Mn_{20}Ni_{15}$ alloy (ΔE = 1.05 V) was broader than that of 304SS; although the i_{pass} for 304SS, 0.02 mA/cm^2, was smaller than that of the $Al_{7.5}Cr_{22.5}Fe_{35}Mn_{20}Ni_{15}$ alloy.

Both of these two alloys had the same breakdown potential of the main passivation region, E_b = 0.98 V (SSE). Figure 4c shows the SEM micrograph of the $Al_{7.5}Cr_{22.5}Fe_{35}Mn_{20}Ni_{15}$ alloy after polarization test. The major corrosion region was the BCC dendrite matrix; the precipitates and the interdendrites were almost unchanged, and the scratches on the interdendrites due to the polish were still visible. Therefore, 1M H_2SO_4 solution corroded BCC dendrites rather than ordered BCC precipitates and FCC interdendrites in the alloy.

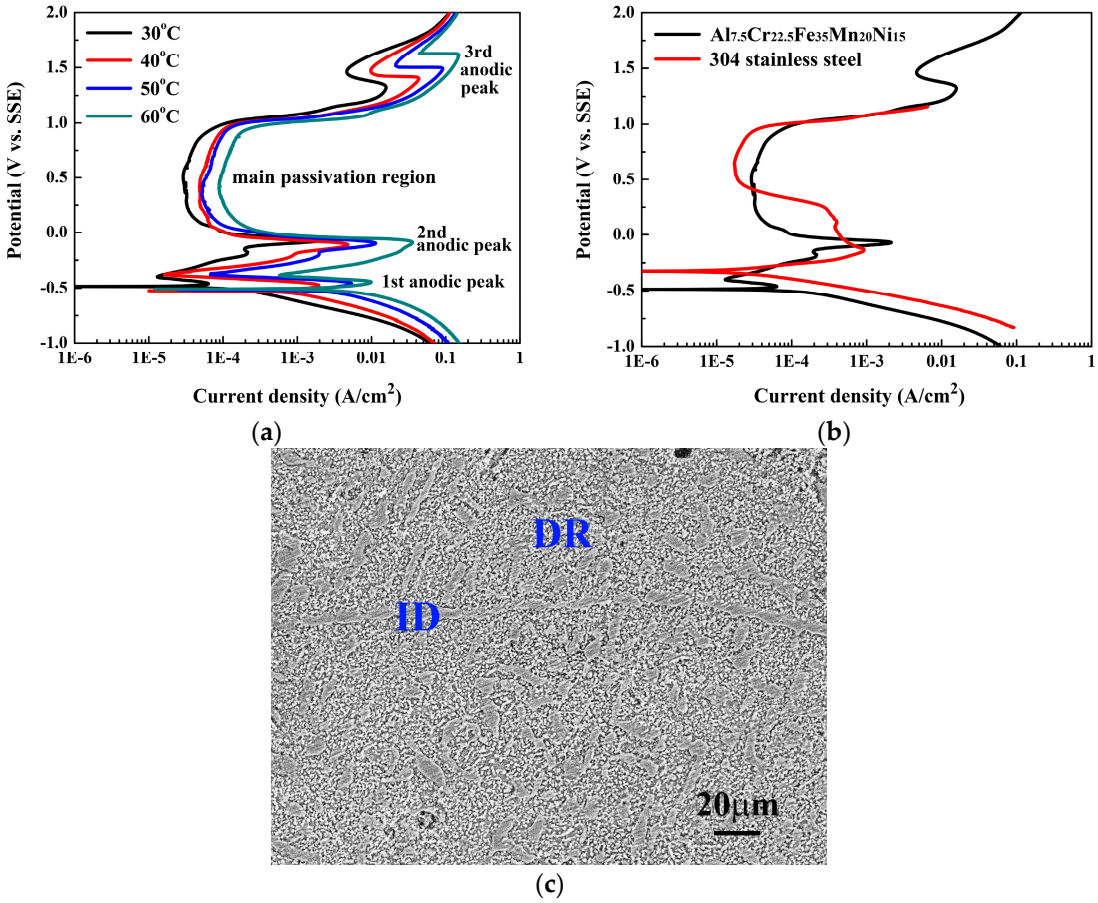

Figure 4. Polarization behaviors of the $Al_{7.5}Cr_{22.5}Fe_{35}Mn_{20}Ni_{15}$ alloy in 1M H_2SO_4 solution, (**a**) polarization curves of the $Al_{7.5}Cr_{22.5}Fe_{35}Mn_{20}Ni_{15}$ alloy measured at different temperatures; (**b**) polarization curves of the $Al_{7.5}Cr_{22.5}Fe_{35}Mn_{20}Ni_{15}$ alloy and 304SS at 30 °C; and (**c**) a SEM micrograph of the $Al_{7.5}Cr_{22.5}Fe_{35}Mn_{20}Ni_{15}$ alloy after polarization test indicates that the corrosion area is dendrite matrix.

Table 2. Polarization data of the $Al_{7.5}Cr_{22.5}Fe_{35}Mn_{20}Ni_{15}$ high entropy alloy in 1M H_2SO_4 solution at different temperatures.

	30 °C	40 °C	50 °C	60 °C
E_{corr} (V vs. SSE)	−0.49	−0.52	−0.52	−0.51
i_{corr} (mA/cm^2)	0.13	0.45	2.81	7.28
E_{pp} (V vs. SSE)	−0.46	−0.47	−0.46	−0.44
i_{pp} (mA/cm^2)	0.06	2.05	5.39	4.03
E_{sp} (V vs. SSE)	−0.07	−0.12	−0.10	−0.09
i_{sp} (mA/cm^2)	2.10	4.76	11.24	34.86
i_{pass} (mA/cm^2)	0.03	0.05	0.05	0.09
E_b (V vs. SSE)	0.98	0.98	0.98	0.98
E_{tp} (V vs. SSE)	1.46	1.47	1.50	1.62
i_{tp} (mA/cm^2)	15.36	44.06	92.49	147.73

Figure 5 shows the polarization behaviors of the $Al_{7.5}Cr_{22.5}Fe_{35}Mn_{20}Ni_{15}$ alloy in 1M deaerated HNO_3 solution and the SEM micrograph of the alloy after the polarization test. The polarization behaviors of the $Al_{7.5}Cr_{22.5}Fe_{35}Mn_{20}Ni_{15}$ alloy in 1M HNO_3 solution at different temperatures are shown in Figure 5a, and Table 3 lists the data from which curves are plotted. The E_{corr} of the $Al_{7.5}Cr_{22.5}Fe_{35}Mn_{20}Ni_{15}$ alloy in 1M HNO_3 solution increased markedly from −0.24 to −0.15 V (SSE) when the temperature increased from 30 to 60 °C. The i_{corr} also increased significantly with increasing temperature. The E_{pp} and i_{pp} only slightly changed in this temperature range. The anodic started to fall down and form the passive region after the end of the first anodic peak. However, two anodic peaks were observed in each polarization curve; the passivation region for each curve was thus divided into two sub-domains, and the first sub-domain was the main passivation region for each polarization curve. The i_{pass} for the main passivation regions also slightly increased with increasing temperature, and the E_b of the main passivation regions for the polarization curves only slightly changed with increasing temperature.

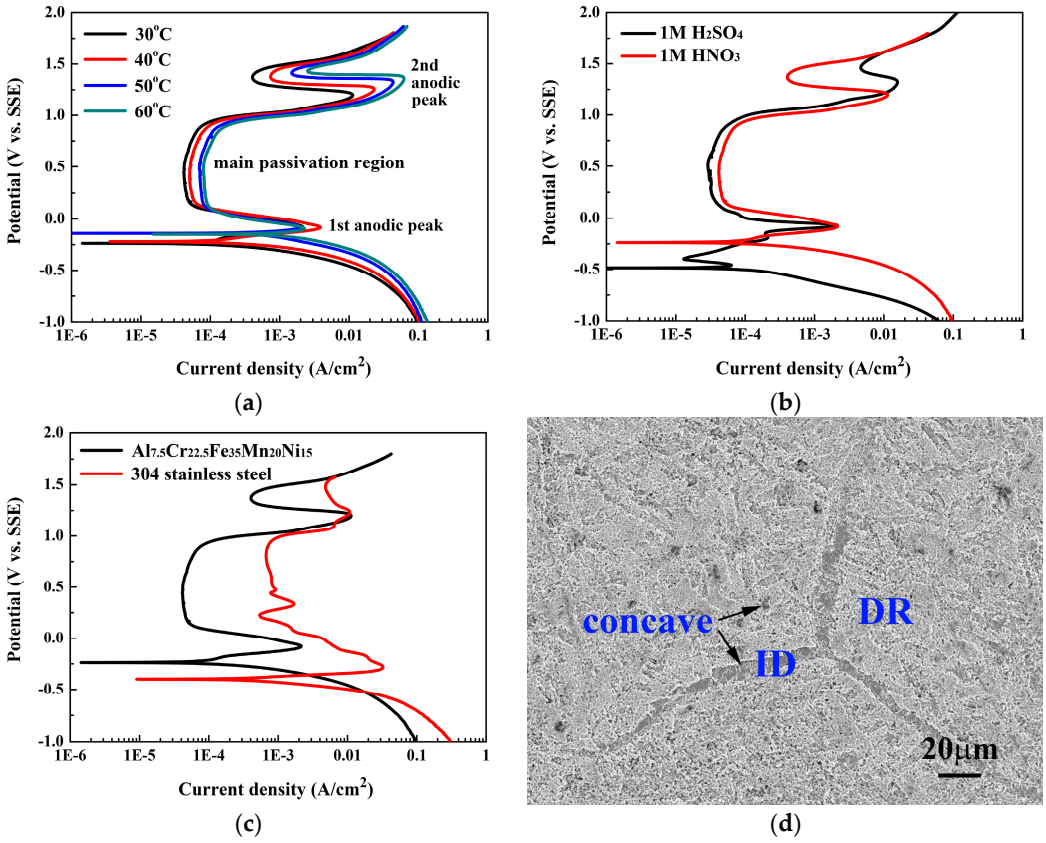

Figure 5. Polarization behaviors of the $Al_{7.5}Cr_{22.5}Fe_{35}Mn_{20}Ni_{15}$ alloy in 1M HNO_3 solution, (**a**) polarization curves of the $Al_{7.5}Cr_{22.5}Fe_{35}Mn_{20}Ni_{15}$ alloy measured at different temperatures; (**b**) polarization curves of the $Al_{7.5}Cr_{22.5}Fe_{35}Mn_{20}Ni_{15}$ alloy in both of 1M H_2SO_4 and 1M HNO_3 solutions at 30 °C; (**c**) polarization curves of the $Al_{7.5}Cr_{22.5}Fe_{35}Mn_{20}Ni_{15}$ alloy and 304SS at 30 °C; and (**d**) a SEM micrograph of the $Al_{7.5}Cr_{22.5}Fe_{35}Mn_{20}Ni_{15}$ alloy after polarization test shows the concave areas are interdendrites and interdendrite fragments of the alloy.

Figure 5b shows the polarization curves of the $Al_{7.5}Cr_{22.5}Fe_{35}Mn_{20}Ni_{15}$ alloy in both the 1M H_2SO_4 and 1M HNO_3 solutions at 30 °C. It is interesting to note that the polarization behaviors of the $Al_{7.5}Cr_{22.5}Fe_{35}Mn_{20}Ni_{15}$ alloy in 1M H_2SO_4 and 1M HNO_3 solutions are quite similar; because the reactions between the metals and the H_2SO_4 or HNO_3 solution were of similar oxidation behavior. The E_{corr} of the $Al_{7.5}Cr_{22.5}Fe_{35}Mn_{20}Ni_{15}$ alloy in 1M HNO_3 solution was higher than that in 1M H_2SO_4 solution; even higher than the E_{pp} of the alloy in 1M H_2SO_4 solution. The first anodic peak for the alloy

in 1M HNO_3 solution was almost matched with the secondary anodic peak of the alloy in 1M H_2SO_4 solution. The secondary anodic peak of the alloy in 1M HNO_3 solution was close to the third anodic peak of the alloy in 1M H_2SO_4 solution. Therefore, the extent of passivity for the alloy in both of these two solutions were very close.

Table 3. Polarization data of the $Al_{7.5}Cr_{22.5}Fe_{35}Mn_{20}Ni_{15}$ high entropy alloy in 1M HNO_3 solution at different temperatures.

	30 °C	40 °C	50 °C	60 °C
E_{corr} (V vs. SSE)	−0.24	−0.22	−0.15	−0.15
i_{corr} (mA/cm^2)	0.67	1.08	1.49	2.59
E_{pp} (V vs. SSE)	−0.08	−0.08	−0.08	−0.10
i_{pp} (mA/cm^2)	2.20	3.90	2.03	2.30
i_{pass} (mA/cm^2)	0.04	0.05	0.07	0.08
E_b (V vs. SSE)	0.97	0.96	0.94	0.93
E_{sp} (V vs. SSE)	1.20	1.27	1.36	1.39
i_{sp} (mA/cm^2)	11.06	23.36	44.58	64.12

Figure 5c compares the polarization curves for the $Al_{7.5}Cr_{22.5}Fe_{35}Mn_{20}Ni_{15}$ alloy and 304SS in 1M HNO_3 solution at 30 °C. The E_{corr} for 304SS, −0.41 V (SSE), was lower than that of the $Al_{7.5}Cr_{22.5}Fe_{35}Mn_{20}Ni_{15}$ alloy; and the i_{corr} for 304SS was larger than that of the $Al_{7.5}Cr_{22.5}Fe_{35}Mn_{20}Ni_{15}$ alloy. In addition, the main passivation region of the $Al_{7.5}Cr_{22.5}Fe_{35}Mn_{20}Ni_{15}$ alloy was broader than that of 304SS; the i_{pass} of the $Al_{7.5}Cr_{22.5}Fe_{35}Mn_{20}Ni_{15}$ alloy was also smaller than that of 304SS. The E_b of the main passivation regions of both alloys were quite close. All of these data indicated that the $Al_{7.5}Cr_{22.5}Fe_{35}Mn_{20}Ni_{15}$ alloy had a better corrosion resistance than 304SS in 1M HNO_3 solution. Figure 5d shows the SEM micrograph of the $Al_{7.5}Cr_{22.5}Fe_{35}Mn_{20}Ni_{15}$ alloy after the polarization test. The micrograph reveals that the entire surface was corroded. However, the FCC interdendrites were concave and there was a large number of small holes; which indicated that the corrosion resistance of both the FCC interdendrites and the ordered BCC precipitates were less than that of the BCC dendrites in 1M HNO_3 solution.

Figure 6 shows the polarization behaviors of the $Al_{7.5}Cr_{22.5}Fe_{35}Mn_{20}Ni_{15}$ alloy in 1M deaerated HCl solution and the SEM micrograph of the alloy after the polarization test. The polarization behaviors of the $Al_{7.5}Cr_{22.5}Fe_{35}Mn_{20}Ni_{15}$ alloy in 1M HCl solution at different temperatures are shown in Figure 6a. The shapes of the polarization curves of the $Al_{7.5}Cr_{22.5}Fe_{35}Mn_{20}Ni_{15}$ alloy in 1M HCl solution are different in comparison to that in 1M H_2SO_4 and 1M HNO_3 solutions; because the corrosion mechanism of the alloy in 1M HCl solution included the attack of chlorine ions, and reaction in an acidic solution. Table 4 lists the data from which the curves are plotted. The E_{corr} and i_{corr} both increased with increasing temperature; the highest value of i_{corr} of the $Al_{7.5}Cr_{22.5}Fe_{35}Mn_{20}Ni_{15}$ alloy in 1M HCl solution also revealed the highest corrosion rate of the alloy in these three solutions. Two anodic peaks exist in the polarization curve tested at 30 °C, whereas only one anodic peak exists in the polarization curve tested at 40 °C, and the anodic peak is almost eliminated when the temperature reached 50 °C. The polarization curves for the alloy in 1M HCl solution had a narrower passivation region than that in the other solutions, and the passivation region became smaller with increasing temperature.

Figure 6b compares the polarization curves of the $Al_{7.5}Cr_{22.5}Fe_{35}Mn_{20}Ni_{15}$ alloy and 304SS in 1M HCl solution at 30 °C. The E_{corr} for 304SS, −0.51 V (SSE), was higher than that of the $Al_{7.5}Cr_{22.5}Fe_{35}Mn_{20}Ni_{15}$ alloy, and the i_{corr} for 304SS, 2.0 mA/cm^2, was also smaller than that of the $Al_{7.5}Cr_{22.5}Fe_{35}Mn_{20}Ni_{15}$ alloy. The polarization curves for these two alloys indicated that 304SS had better corrosion resistance than the $Al_{7.5}Cr_{22.5}Fe_{35}Mn_{20}Ni_{15}$ alloy in 1M HCl solution. Figure 6c shows the SEM micrograph of the $Al_{7.5}Cr_{22.5}Fe_{35}Mn_{20}Ni_{15}$ alloy after the polarization test. The micrograph also reveals that the entire surface was corroded. The FCC interdendrites were concave; a large number of small holes indicated the loss of ordered BCC precipitates; and some bigger holes indicated pitting

due to the attack of chlorine ions. However, the SEM micrograph indicated that corrosion resistance of both of the FCC interdendrites and the ordered BCC precipitates were less than that of the BCC dendrites in 1M HCl solution.

Table 4. Polarization data of the $Al_{7.5}Cr_{22.5}Fe_{35}Mn_{20}Ni_{15}$ high entropy alloy in 1M HCl solution at different temperatures

	30 °C	40 °C	50 °C	60 °C
E_{corr} (V vs. SSE)	−0.55	−0.48	−0.46	−0.43
i_{corr} (mA/cm^2)	4.50	7.50	8.95	11.36
E_{pp} (V vs. SSE)	−0.44	−0.40	-	-
i_{pp} (mA/cm^2)	4.48	7.00	-	-
i_{pass} (mA/cm^2)	1.00	3.65	-	-
E_{sp} (V vs. SSE)	−0.31	-	-	-
i_{sp} (mA/cm^2)	2.00	-	-	-
E_b (V vs. SSE)	−0.26	−0.30	-	-

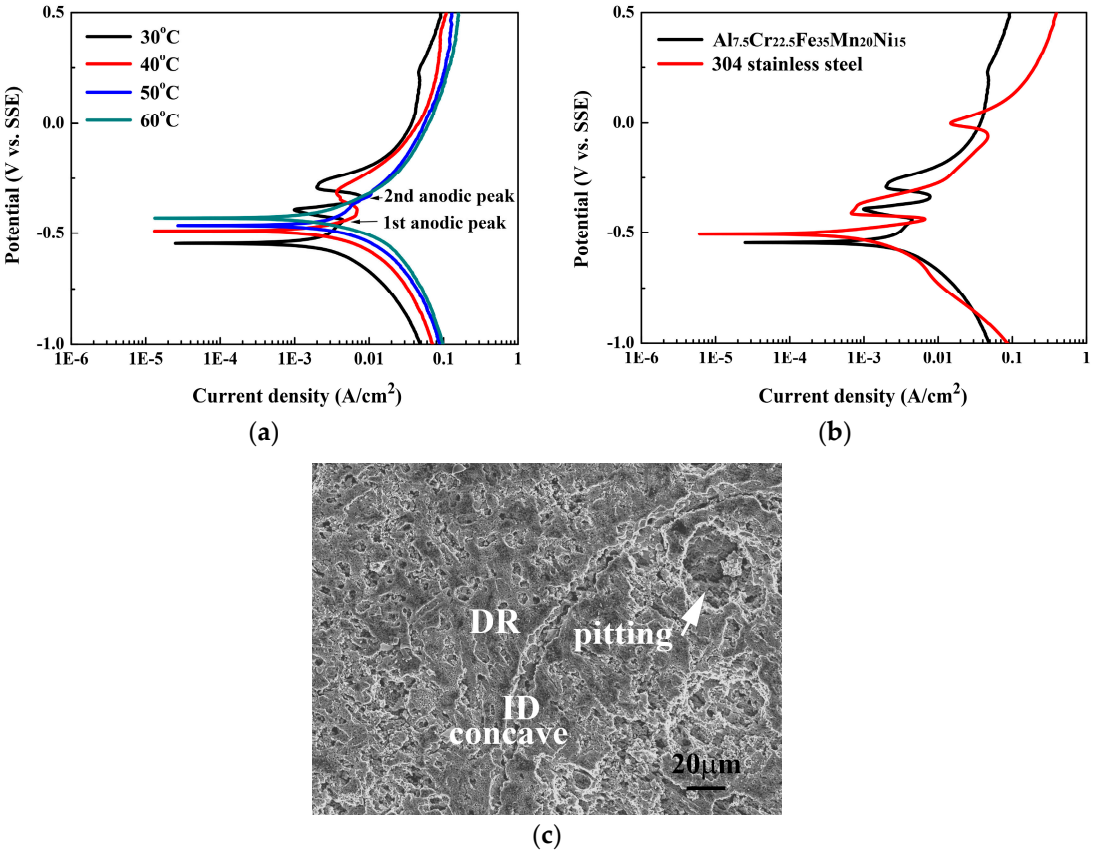

Figure 6. Polarization behaviors of the $Al_{7.5}Cr_{22.5}Fe_{35}Mn_{20}Ni_{15}$ alloy in 1M HCl solution, (**a**) polarization curves of the $Al_{7.5}Cr_{22.5}Fe_{35}Mn_{20}Ni_{15}$ alloy measured at different temperatures; (**b**) polarization curves of the $Al_{7.5}Cr_{22.5}Fe_{35}Mn_{20}Ni_{15}$ alloy and 304SS at 30 °C; and (**c**) a SEM micrograph of the $Al_{7.5}Cr_{22.5}Fe_{35}Mn_{20}Ni_{15}$ alloy after the polarization test shows the concave areas are interdendrites and interdendrite fragments of the alloy.

The polarization behaviors of the $Al_{7.5}Cr_{22.5}Fe_{35}Mn_{20}Ni_{15}$ alloy in 1M NaCl solution, and in the mixed solution of 1M NaCl and 1M H_2SO_4, were also studied to understand the effect of chlorine ions on the passive film. Figure 7a presents the polarization curves of the $Al_{7.5}Cr_{22.5}Fe_{35}Mn_{20}Ni_{15}$ alloy in the 1M H_2SO_4 acid, 1M NaCl solution, and the mixed solution of 1M NaCl and 1M H_2SO_4 at 30 °C. Table 5 lists the data from which the curves are plotted. The E_{corr} of the $Al_{7.5}Cr_{22.5}Fe_{35}Mn_{20}Ni_{15}$

alloy in the mixed solution of 1M NaCl and 1M H_2SO_4 was almost the same as the alloy in 1M H_2SO_4 solution; but the i_{corr} increased significantly, from 0.13 to 8.00 mA/cm^2. Both the E_{pp} and E_{sp} for the alloy in the mixed solution of 1M NaCl and 1M H_2SO_4 were slightly higher than that in the 1M H_2SO_4 solution; but the i_{pp} and i_{sp} were also markedly increased. The shape of the passivation region was also seriously destroyed by the attack of chlorine ions; the extent of passivity thus decreased. Moreover, the polarization curve of the alloy in 1M NaCl solution indicated that no passivation region was observed.

Figure 7b compares the polarization curves of the $Al_{7.5}Cr_{22.5}Fe_{35}Mn_{20}Ni_{15}$ alloy and 304SS in 1M NaCl solution at 30 °C. The E_{corr} for 304SS, −0.86 V (SSE), was lower than that of the $Al_{7.5}Cr_{22.5}Fe_{35}Mn_{20}Ni_{15}$ alloy, and the i_{corr} for 304SS, 0.07 mA/cm^2, was higher than that of the $Al_{7.5}Cr_{22.5}Fe_{35}Mn_{20}Ni_{15}$ alloy. Additionally, the E_b for 304SS, −0.02 V (SSE), was higher than that of the $Al_{7.5}Cr_{22.5}Fe_{35}Mn_{20}Ni_{15}$ alloy, indicated that 304SS had better pitting resistance than the $Al_{7.5}Cr_{22.5}Fe_{35}Mn_{20}Ni_{15}$ alloy. Figure 7c,d show the SEM micrographs of the $Al_{7.5}Cr_{22.5}Fe_{35}Mn_{20}Ni_{15}$ alloy after the polarization test in the mixed solution of 1M NaCl and 1M H_2SO_4, and 1M NaCl solution, respectively. Figure 7c shows two types of corrosion; one is the corrosion in the BCC dendrite matrix because of H_2SO_4; the other is pitting due to NaCl. This micrograph also proves that the FCC interdendrites were not corroded after the polarization test in 1M H_2SO_4 solution. Figure 7d shows that only pitting was observed on the surface of the alloy after the polarization test in 1M NaCl solution.

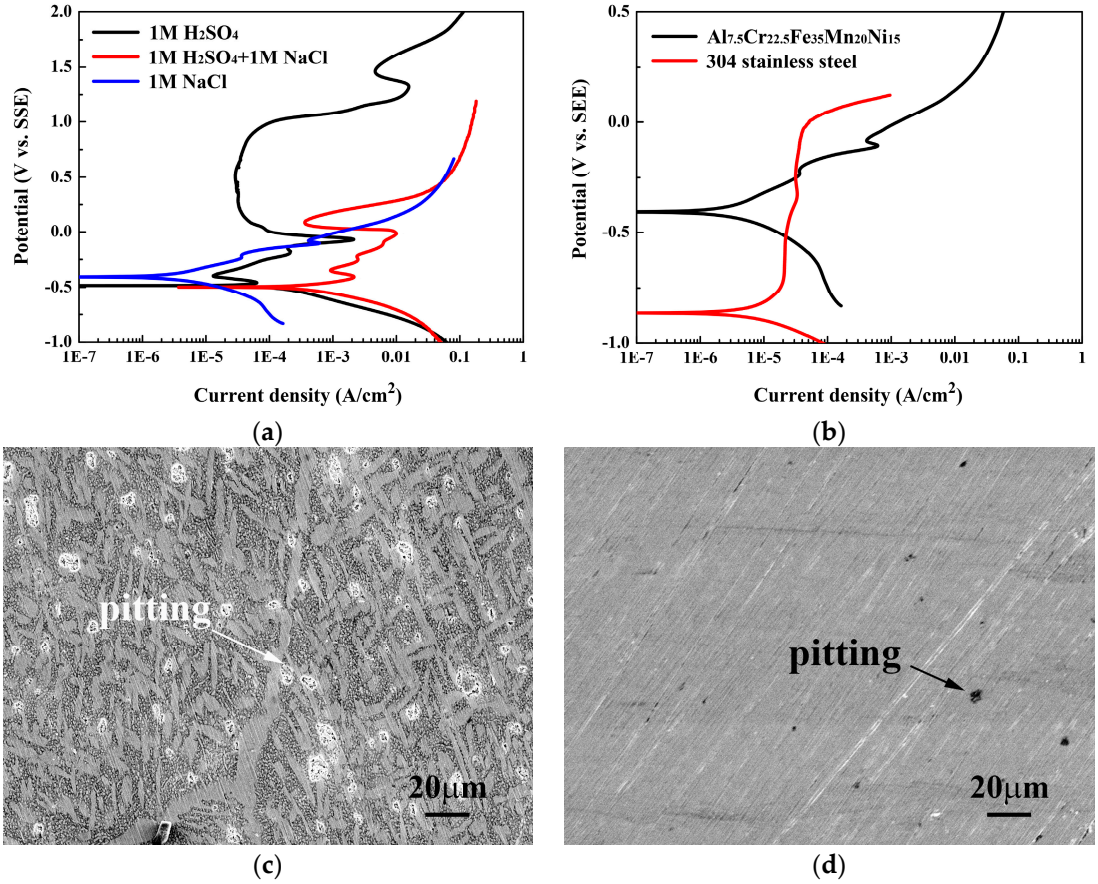

Figure 7. Polarization behaviors of the $Al_{7.5}Cr_{22.5}Fe_{35}Mn_{20}Ni_{15}$ alloy, (**a**) polarization curves of the $Al_{7.5}Cr_{22.5}Fe_{35}Mn_{20}Ni_{15}$ alloy in 1M H_2SO_4 acid, 1M NaCl and the mixed solution of 1M NaCl and 1M H_2SO_4 at 30 °C; (**b**) polarization curves of the $Al_{7.5}Cr_{22.5}Fe_{35}Mn_{20}Ni_{15}$ alloy and 304SS at 30 °C; (**c**) a SEM micrograph of the $Al_{7.5}Cr_{22.5}Fe_{35}Mn_{20}Ni_{15}$ alloy after the polarization test in the mixed solution of 1M H_2SO_4 and 1M NaCl; and (**d**) a SEM micrograph of the $Al_{7.5}Cr_{22.5}Fe_{35}Mn_{20}Ni_{15}$ alloy after the polarization test in 1M NaCl solution.

Table 5. Polarization data of the $Al_{7.5}Cr_{22.5}Fe_{35}Mn_{20}Ni_{15}$ high entropy alloy in the 1M H_2SO_4 and 1M NaCl solutions, and mixed solution of 1M H_2SO_4 and 1M NaCl at 30 °C

	1M H_2SO_4	**1M H_2SO_4 + 1M NaCl**	**1M NaCl**
E_{corr} (V vs. SSE)	−0.49	−0.50	−0.41
i_{corr} (mA/cm^2)	0.13	8.00	0.01
E_{pp} (V vs. SSE)	−0.46	−0.40	-
i_{pp} (mA/cm^2)	0.06	2.10	-
E_{sp} (V vs. SSE)	−0.07	−0.01	-
i_{sp} (mA/cm^2)	2.10	10.00	-
i_{pass} (mA/cm^2)	0.03	0.04	-
E_b (V vs. SSE)	0.98	0.20	-
E_{tp} (V vs. SSE)	1.46	-	-
i_{tp} (mA/cm^2)	15.36	-	-

4. Conclusions

1. The $Al_{7.5}Cr_{22.5}Fe_{35}Mn_{20}Ni_{15}$ high-entropy alloy has a dendritic structure. There were three phases present in the alloy, FCC-structured interdendrites, BCC-structured dendrites, and ordered BCC-structured precipitates dispersed in the dendrite matrix. The lattice constants of the FCC and BCC phases were 0.360 nm and 0.287 nm, respectively. In addition, the ordered BCC precipitates were coherent with the BCC dendrite matrix, and had the same lattice constant of 0.287 nm.

2. The polarization curves of the $Al_{7.5}Cr_{22.5}Fe_{35}Mn_{20}Ni_{15}$ alloy had three anodic peaks in 1M H_2SO_4 solution, and the passivation regions were divided into three sub-domains. The polarization curves of the alloy had two anodic peaks in 1M HNO_3 solution, and the passivation regions were divided into two sub-domains. The formation of the anodic peaks was due to the iron, cobalt, and nickel hydroxide that occurred through the dissolution and precipitation mechanism. The passivation region of the alloy was also divided into two sub-domains in 1M HCl solution at 30 °C; but the anodic peaks and the passivation regions disappeared when the temperature reached 50 °C.

3. By comparing the polarization curves of the $Al_{7.5}Cr_{22.5}Fe_{35}Mn_{20}Ni_{15}$ alloy and 304SS, the corrosion resistance of the $Al_{7.5}Cr_{22.5}Fe_{35}Mn_{20}Ni_{15}$ alloy was found to be almost similar to 304SS in both the 1M H_2SO_4 solution and 1M HCl solution. The corrosion resistance of the $Al_{7.5}Cr_{22.5}Fe_{35}Mn_{20}Ni_{15}$ alloy was much better than 304SS in 1M HNO_3 solution. However, the corrosion resistance of the $Al_{7.5}Cr_{22.5}Fe_{35}Mn_{20}Ni_{15}$ alloy was less than 304SS in 1M NaCl solution.

4. After the polarization test, BCC dendrites were the first to corrode in the 1M H_2SO_4 solution rather than the FCC interdendrites and the ordered BCC precipitates. The entire surface was corroded in both the 1M HNO_3 and 1M HCl solutions, but the FCC interdendrites and the ordered BCC precipitates were corroded more seriously. However, many pitting holes were observed after the polarization test in 1M NaCl solution.

Acknowledgments: The authors would like to thank the Yeh group for providing the specimens. Also, the authors would like to thank the Ministry of Science and Technology of the Republic of China, Taiwan for financially supporting part of this research under Contract No. NSC 100-2221-E-034-009.

Author Contributions: Chun-Huei Tsau conceived and designed the experiments; Po-Yen Lee and Chun-Huei Tsau performed the experiments; Po-Yen Lee and Chun-Huei Tsau analyzed the data; Chun-Huei Tsau contributed reagents/materials/analysis tools; Chun-Huei Tsau wrote the paper. Both authors have read and approved the final manuscript.

Conflicts of Interest: The authors declare no conflict of interest.

References

1. Huang, P.K.; Yeh, J.W.; Shun, T.T.; Chen, S.K. Multi-Principal-Element Alloys with Improved Oxidation and Wear Resistance for Thermal Spray Coating. *Adv. Eng. Mater.* **2004**, *6*, 74–78. [CrossRef]

2. Yeh, J.W.; Chen, S.K.; Gan, J.Y.; Chin, T.S.; Shun, T.T.; Tsau, C.H.; Chang, S.Y. High-entropy alloys with multi-principal elements: Novel alloy design concepts and outcomes. *Adv. Eng. Mater.* **2004**, *6*, 299–303. [CrossRef]
3. Murty, B.S.; Yeh, J.W.; Ranganathan, S. *High-Entropy Alloys*; Elsevier: London, UK, 2014; pp. 1–35.
4. Zhang, Y.; Lu, Z.P.; Ma, S.G.; Liaw, P.K.; Tang, Z.; Cheng, Y.Q.; Gao, M.C. Guidelines in predicting phase formation of high-entropy alloys. *MRS Commun.* **2014**, *4*, 57–62. [CrossRef]
5. Zhang, S.; Wu, C.L.; Yi, J.Z.; Zhang, C.H. Synthesis and characterization of FeCoCrAlCu high-entropy alloy coating by laser surface alloying. *Surf. Coat. Technol.* **2015**, *262*, 64–69. [CrossRef]
6. Dolique, V.; Thomann, A.L.; Brault, P.; Tessier, Y.; Gillon, P. Thermal stability of AlCoCrCuFeNi high entropy alloy thin films studied by in-situ XRD analysis. *Surf. Coat. Technol.* **2010**, *204*, 1989–1992. [CrossRef]
7. Senkov, O.N.; Wilks, G.B.; Scott, J.M.; Miracle, D.B. Mechanical properties of $Nb_{25}Mo_{25}Ta_{25}W_{25}$ and $V_{20}Nb_{20}Mo_{20}Ta_{20}W_{20}$ refractory high entropy alloys. *Intermetallics* **2011**, *19*, 698–706. [CrossRef]
8. Lilensten, L.; Couzinié, J.P.; Perrière, L.; Bourgon, J.; Emery, N.; Guillot, I. New structure in refractory high-entropy alloys. *Mater. Lett.* **2014**, *132*, 123–125. [CrossRef]
9. Wang, W.H. High-entropy metallic glasses. *JOM* **2014**, *66*, 2067–2077. [CrossRef]
10. Chen, Y.Y.; Hong, U.T.; Shih, H.C.; Yeh, J.W.; Duval, T. Electrochemical kinetics of the high entropy alloys in aqueous environments - comparison with type 304 stainless steel. *Corros. Sci.* **2005**, *47*, 2679–2699. [CrossRef]
11. Qiu, X.W.; Zhang, Y.P.; Hea, L.; Liu, C.G. Microstructure and corrosion resistance of AlCrFeCuCo high entropy alloy. *J. Alloy. Compd.* **2013**, *549*, 195–199. [CrossRef]
12. Li, J.M.; Yang, X.; Zhu, R.L.; Zhang, Y. Corrosion and Serration Behaviors of $TiZr_{0.5}NbCr_{0.5}V_xMoy$ High Entropy Alloys in Aqueous Environments. *Metals* **2014**, *4*, 597–608. [CrossRef]
13. Chen, S.T.; Tang, W.Y.; Kuo, Y.F.; Chen, S.Y.; Tsau, C.H.; Shun, T.T.; Yeh, J.W. Microstructure and properties of age-hardenable $Al_xCrFe_{1.5}MnNi_{0.5}$ alloys. *Mater. Sci. Eng. A* **2010**, *547*, 5818–5825. [CrossRef]
14. Lee, C.P.; Chen, Y.Y.; Hsu, C.Y.; Yeh, J.W.; Shih, H.C. Enhancing pitting corrosion resistance of $Al_xCrFe_{1.5}MnNi_{0.5}$ high-entropy alloys by anodic treatment in sulfuric acid. *Thin Solid Films* **2008**, *517*, 1301–1305. [CrossRef]
15. Revie, R.W.; Uhlig, H.H. *Corrosion and Corrosion Control*, 4th ed.; John Wiley & Sons: New York, NJ, USA, 2008; p. 36.
16. Bates, R.G.; MacAskill, J.B. Standard Potential of the Silver-Silver Chloride Electrode. *Pure Appl. Chem.* **1978**, *50*, 1701–1706. [CrossRef]
17. Abdallah, M. Corrosion behavior of 304 stainless steel in sulphuric acid solutions and its inhibition by some substituted pyrazolones. *Mater. Chem. Phys.* **2003**, *81*, 786–792. [CrossRef]
18. Ashworth, V.; Boden, P.J. Potential-pH diagrams at elevated temperatures. *Corros. Sci.* **1970**, *10*, 709–718. [CrossRef]
19. Clayton, C.R.; Lu, Y.C. A Bipolar Model of the Passivity of Stainless Steel: The Role of Mo Addition. *J. Electrochem. Soc.* **1986**, *133*, 2465–2473. [CrossRef]